Investigation on the methane adsorption capacity in coals: considerations from nanopores by multifractal analysis

Journal:	*Energy & Fuels*
Manuscript ID	ef-2021-00238d.R1
Manuscript Type:	Article
Date Submitted by the Author:	09-Mar-2021
Complete List of Authors:	Li, Qian; China University of Geosciences Beijing Liu, Dameng; China University of Geosciences Beijing, Energy Resources Cai, Yidong; China University of Geosciences Beijing, Zhou, Yingfang; University of Aberdeen, School of Engineering Yin, Tingting ; China University of Geosciences Beijing

Investigation on the methane adsorption capacity in coals: considerations from nanopores by multifractal analysis

Qian Li [a, b], Dameng Liu [a, b], Yidong Cai [a,b*], Yingfang Zhou [c], Tingting Yin [a,b]

[a]*School of Energy Resources, China University of Geosciences, Beijing 100083, China*

[b]*Coal Reservoir Laboratory of National Engineering Research Center of CBM Development & Utilization, China University of Geosciences, Beijing 100083, China*

[c]*School of Engineering, Fraser Noble Building, King's College, University of Aberdeen, AB24 3UE Aberdeen, UK*

ABSTRACT:

Methane adsorption properties of coal are essential for coalbed methane (CBM) extraction and clean energy utilization. However, the effect of nanopores on CH_4 adsorption in high volatile bituminous coal and anthracite remains to be revealed. In this work, the multi-dimensional description of nanopores was established using gas adsorption and FIB-SEM experiments. And the heterogeneous features at different sizes were finely quantified by multifractal analysis. Results show that the pores with size smaller than 100 nm, as storage section, are isolated in the space. The nanopores of the sample LHG have stronger heterogeneity in multiple dimensions. The pore size distributions with apparent aggregation are composed of 0.45-0.70 nm (from CO_2 adsorption), 2-50 nm (from N_2 adsorption) and 10-50 nm (from FIB-SEM). Nanopore structure affects the adsorption capacity of CH_4 mainly in micropore structure, pore morphology and heterogeneity. The well-developed micropore structure is conducive to methane enrichment. The ink-bottle pores with the higher specific surface area are beneficial to gas storage, whereas plate-like/slit-like pores will facilitate the desorption and diffusion of gas. The more robust pore heterogeneity in the range of 0.45-0.70

* Corresponding author, Email address: yidong.cai@cugb.edu.cn (Y. Cai)

nm and 2-50 nm significantly contribute to methane adsorption. This work may allow significant insights into the interaction of coal with gases during enhancing CBM recovery.

Keywords: Coalbed methane; Nanopore; Adsorption; FIB-SEM; Multifractal analysis

1. INTRODUCTION

Coalbed methane (CBM) reservoir has been a hotspot as a result of the development of greenhouse gas control and clean energy utilization. Methane is generally stored in coal by the adsorption mechanism [1]. The adsorption behavior may restrict the production of CBM reservoirs and threaten the safety of the coal mining process [2-5]. Due to the different physical and chemical properties of coals, the governing factors of CH_4 adsorption capacity are quite complicated [6-15]. An emerging number of studies on methane adsorption has been carried out, focusing on coal rank, temperature, moisture content and coal composition [6-12]. Besides, many current pieces of research noticed the influence of pore structure on gas adsorption, including pore specific surface area (SSA) [13, 14], pore volume [15, 16], pore size distribution (PSD) [17, 18] and surface roughness [19, 20]. The International Union of Pure and Applied Chemistry (IUPAC) established the classification consisting of micropores (<2 nm), mesopores (2-50 nm) and macropores (>50 nm) [21]. Nanopore with the pore size smaller than 100 nm, as an essential component in the pore-fracture structure, will significantly affect the adsorption mechanism [19, 22, 23]. However, there are still many controversies about the control effect of methane adsorption capacity [24]. For example, regarding the effect of SSA of the micropores, some scholars believed that the larger SSA will provide more adsorption sites, hence the CH_4 adsorption capacity will be higher [13, 14]. But Byamba investigated that the comparison chart of BET-SSA and CH_4 adsorption capacity may be invalid in the microporous adsorbent [25].

The commonly used methods for characterizing nanopore structure in coal contain mercury intrusion porosimetry (MIP) and gas adsorption (CO_2 and N_2). The MIP method can assess the porosity distribution with size above 3 nm [26], whereas the coal matrix will be compressed and the narrow pores will be damaged at the applied pressure > 10 MPa [27]. Gas adsorption (CO_2 and N_2) is more advantageous for the analysis of nanopores. Low-temperature N_2 adsorption is powerful for evaluating mesopores and parts of macropores [28], but cannot effectively access the features of micropores. The CO_2 molecule is endowed with high saturated vapor pressure and fast diffusion speed at 273 K [29]. Meanwhile, CO_2 with a kinetic diameter of 0.33 nm is allowed to enter pores less than 1 nm, thus it is usually used as an ideal gas for analyzing micropores of coal. The combination of CO_2 and N_2 adsorption methods can characterize the nearly full nano-scale pore structure. However, subjecting to the test mechanism constraints, the spatial distribution is difficult to be obtained. Therefore, advanced techniques including X-ray nano-tomography (Nano-CT) and focused ion beam-scanning electron microscopy (FIB-SEM) are also introduced to evaluate the pore structure [30]. The latter is chosen in this work because of its higher resolution (~ 10nm/pixel).

This work aims at shedding light on the following issues: 1) multi-dimensional description of nanopores through gas adsorption (CO_2 and N_2) and FIB-SEM techniques; 2) the multi-heterogeneity of nanopore structures by multifractal analysis; 3) the effect of nanopores on CH_4 adsorption.

2. MATERIAL AND METHODS

2.1. Coal Sampling and Analysis

One high volatile bituminous coal and one anthracite were collected from the Junggar Basin and Qinshui Basin of China, which were carefully packaged and then transported to the laboratory for

experiments. A summary of the sample information, including maximum vitrinite reflectance ($R_{o,m}$), helium porosity, maceral and proximate analysis, is provided in Table 1. The standards used in these tests are the Chinese National Standard GB/T 6948-2008 ($R_{o,m}$), the Chinese Oil and Gas Industry Standard SY/T 5336-1996 (helium porosimetry test), the Scheme of the International Committee of Coal Petrology (coal macerals)[31] and the Standard of ASTM D7582-15 (proximate analysis). Detailed experiment procedure is displayed in our previous research [27]. The initial cubic samples with ~0.5 cm × 1 cm × 1 cm were adopted in the FIB-SEM tomography. The samples used in the gas adsorption (CH_4, CO_2 and N_2) experiments were the powder samples of 60-80 mesh.

Table 1. Properties of selected coal samples

Sample ID	$R_{o,m}$ (%)	Basins	Maceral and mineral (vol%)				Porosity (%)	Permeability (mD)	Langmuir parameters	
			V	I	E	M			V_L (m^3/t)	P_L (MPa)
LHG	0.98	Junggar	53.40	19.70	0.37	26.50	9.56	0.21	35.98	0.71
L-1	2.73	Qinshui	66.80	14.40	0.00	18.80	5.37	0.011	34.81	1.06

Note: V- Vitrinite; I - Inertinite; E - Exinite; M- Mineral.

2.2. Gas Adsorption Experiments and FIB-SEM Tomography

The gas adsorption experiments were carried by CO_2 adsorption, low-temperature N_2 adsorption/desorption, and CH_4 isotherm adsorption. The coal samples of 60-80 mesh first dried for 48 h. Both CO_2 adsorption and low-temperature N_2 adsorption/desorption measurements were performed with a Micromeritics ASAP-2460 specific surface analyzer. The corresponding temperatures of CO_2 adsorption and low-temperature N_2 adsorption/desorption measurements are 273 K and 77 K, respectively. The density functional theory (DFT) [32] molecular model was adopted herein to obtain the pore size distributions (PSD) from CO_2 adsorption in the range of 0.489-1.083 nm and N_2 adsorption in the range of 2-100 nm, respectively. DFT can be used to better capture the thermodynamic behavior and density distribution of fluids at the molecular level, and then a more

reliable curve of PSD can be assessed [3, 24, 33, 34]. Besides, CH_4 adsorption experiments corroborated the adsorption capacity of the two samples were conducted at 30 ℃ using the TerraTek Isotherm Measurement System (IS-100), obeying the Chinese National Standard of GB/T 19560-2008. The curves of CH_4 adsorption experiments are displayed in Figure 1a. The Langmuir volume (V_L) and Langmuir pressure (P_L) were provided by Langmuir model [35], as shown in eq 1:

$$V = \frac{PV_L}{P + P_L} \quad (1)$$

where V is the volume of adsorbed methane, m^3/t; P is the pressure, MPa; V_L is the Langmuir volume and represents the maximum volume of coal, m^3/t; P_L is the Langmuir pressure corresponding to the 50% of maximum adsorption capacity, which can evaluate the difficulty of adsorbing methane in CBM reservoirs, MPa.

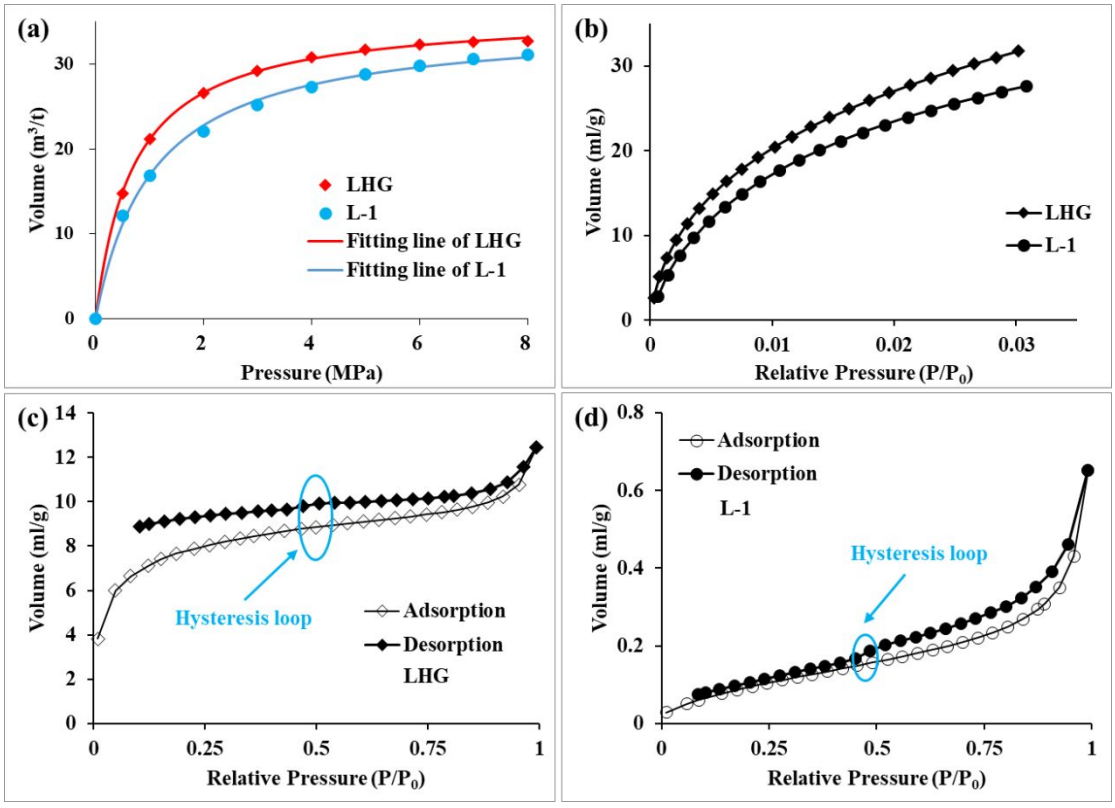

Figure 1. The isotherms of gas adsorption experiments. (a)-CH_4 adsorption, (b)-CO_2 adsorption, (c-d) low-temperature N_2 adsorption/desorption isotherms.

With FIB-SEM tomography when a polished coal sample is exposed to a dual-beam (ion and

electron) system, the selected area is then cut and imaged. The experimental instrument is Zeiss Crossbeam540. The high-resolution images (10 nm/pixel) obtained can make the research scale reach the nanometer level. To perform subsequent multifractal analysis, the size of the studied domains must meet the requirement of being larger than the representative elementary volume (REV) [36]. The sizes of REV have been determined (80 pixels for LHG and 280 pixels for L-1) in our published work [37], so choosing the size of the studied domains to be 512 × 512 × 512 voxels is sufficient.

2.3. Multifractal Analysis

As an extension of fractal theory [38], the multifractal analysis can show more details in complex porous media. The single fractal dimension usually used reflects more the overall characteristics of PSD, rather than focusing on local differences. Multifractal analysis can decompose self-similar measures into interlacing fractal sets and separate the complex fractal structure into several parts [33, 38-40]. And it can be distinguished by the singularity strength and generalized dimension. There are mainly two methods to perform the multifractal analysis including the box-counting method and wavelet method [38], and the former is adopted herein due to the features of pore system in coal [33, 37, 41]. Method in this class obeys the following steps:

First, a series of boxes with the same length ε is used to cover the signal interval and they are labeled with *i*. Besides, $N(\varepsilon)$ represents the number of boxes required completely to overlay the signal interval. In this work, relative pressure data in gas adsorption (CO_2 and N_2) experiments was considered as the signal interval. The probability mass function in the *i*-th box can be defined by eq 2:

$$P_i(\varepsilon) = \frac{N_i(\varepsilon)}{N_t} \tag{2}$$

where $N_i(\varepsilon)$ is the gas adsorption volume in the *i*-th box; N_t is the total gas adsorption volume. $P_i(\varepsilon)$, the probability mass, follows an exponential function with the length ε of the box, which can be expressed as:

$$P_i(\varepsilon) \sim \varepsilon^{\alpha_i} \tag{3}$$

where α_i is the Lipschitz-Hölder singularity exponent, which reflects the local singularity strength of the mass probability function $P_i(\varepsilon)$, and its value is relevant to the current position of the box on the research interval [39].

When the values of α are same, the number of the boxes is marked as $N_\alpha(\varepsilon)$, following the eq 4:

$$N_\alpha(\varepsilon) \propto \varepsilon^{-f(\alpha)} \tag{4}$$

where $f(\alpha)$ is the fractal dimension of the fractal subset labeled by the singularity exponent α. The curve composed of α and $f(\alpha)$ is recorded as the multifractal singularity spectrum, which can indicate the heterogeneous distribution of gas adsorption on the fractal structure, thereby providing more detailed structural information than single fractal. After that, $\alpha(q)$ and $f(\alpha)$ can be determined by the eqs. 5 and 6 proposed by Chhabra and Jensen [42]:

$$\alpha(q) \propto \frac{\left[\sum_{i=1}^{N(\varepsilon)} (u_i(q,\varepsilon) \times \ln p_i(\varepsilon))\right]}{\ln(\varepsilon)} \tag{5}$$

$$f(\alpha) \propto \frac{\left[\sum_{i=1}^{N(\varepsilon)} (u_i(q,\varepsilon) \times \ln u_i(\varepsilon))\right]}{\ln(\varepsilon)} \tag{6}$$

where

$$u_i(q,\varepsilon) = \frac{p_i(\varepsilon)^q}{\sum_{i=1}^{N(\varepsilon)} p_i(\varepsilon)^q} \tag{7}$$

where q is the order of the statistical matrix and ranges from -∞ to +∞. Herein, the value of q is an

integer within [-10, 10] for successive unit steps. When $q > 0$, it represents the high concentration area of the PSD; whereas the low concentration area of PSD is focused for $q < 0$. Besides, the partition function of moment of order q for multifractal analysis can be expressed as eq 8 [42]:

$$u(q,\varepsilon) = \sum_{i=1}^{N(\varepsilon)} p_i(\varepsilon)^q \propto \varepsilon^{\tau(q)} \tag{8}$$

where $\tau(q)$ is the mass scaling function of the order q, which can be calculated by:

$$\tau(q) = -\lim_{\varepsilon \to 0} \frac{\ln \sum_{i=1}^{N(\varepsilon)} p_i(\varepsilon)^q}{\ln(\varepsilon)} \tag{9}$$

The relationship between the generalized dimension (D_q) and the order (q) can be obtained by eq 10 [39]:

$$D_q = \frac{\tau(q)}{q-1} \tag{10}$$

For the monofractal, the relation of D_q and q is a constant and shows no richer information as q changes. In the multifractal analysis, the plot of D_q versus q is not a constant function. In this regard, the most commonly used generalized dimensions are D_0, D_1 and D_2 corresponding to q = 0, 1, 2 [43, 44], which are known as capacity, information (Shannon entropy), and correlation dimensions, respectively. The capacity dimension D_0 can show the global characteristics of the system, which is independent of q and the probability of the pores in the box. The information dimension, D_1, evaluates the degree of disorder in the PSD curves. The larger value of D_1 represents the smaller fluctuation of the local pore volume distribution and the higher uniformity of the pore distribution in each pore size interval. As the correlation dimension, D_2 captures the behavior of the second sampling moment and can indicate the degree of spatial autocorrelation of the measures.

Meanwhile, in order to make the function D_q continuous, D_1 can be acquired by the Law of

Robida when $q = 1$ [45]:

$$D_1 = \lim_{\varepsilon \to 0} \frac{\sum_{i=1}^{N(\varepsilon)} p_i(\varepsilon) \ln p_i(\varepsilon)}{\ln(\varepsilon)} \quad (11)$$

The value of D_1 close to 1 means uniform distribution of the system on all scales; on the contrary, D_1 close to 0 represents a concentration of irregularities in the subset of scales [43]. Subsequently, the calculated D_q and q constitute the generalized multifractal dimension spectrum.

Besides, D_2 also can be defined as eq 12 following Riedi et al. [46]:

$$D_2 = 2H - 1 \quad (12)$$

where H is named as the Hurst exponent, which shows the positive autocorrelation and/or spatial long-range variations [45].

3. RESULTS AND DISCUSSION

3.1. Characteristics of the Nanopores Structures

Figure 1b shows the curves of CO_2 adsorption for the two selected coals, which illustrates the adsorption volume gradually increases under the low-pressure condition. Compared with the results of other studies [16, 24, 47, 48], it can be noticed by the relatively high CO_2 adsorption capacity in our samples, indicating that the samples have a high accessibility of CO_2 and/or the well-developed micropore structure [49]. The curves of N_2 adsorption/desorption at 77 K are displayed in Figure 1c-d, which their shapes conform to the Type II reversible isotherms according to the IUPAC classifications [21]. The isotherms represent the process of unlimited monolayer-multilayer adsorption, and the starting point of the middle linear part means the completed monolayer coverage and the unstart multilayer adsorption [50]. Hysteresis loops with changeable shapes can indicate different types of pores, which may be related to the capillary condensation in the mesopores [27]. The

hysteresis loops appearing in Figure 1c-d can be classified into Type H4 (sample LHG) and Type H3 (sample L-1), respectively [29, 50]. The Type H4 loop can be related with narrow slit-like pores, the more obvious uptake at low P/P_0 being attributed to the filling of the micropores. The Type H3 loop is attributed to the non-grid aggregates of plate-like particles.

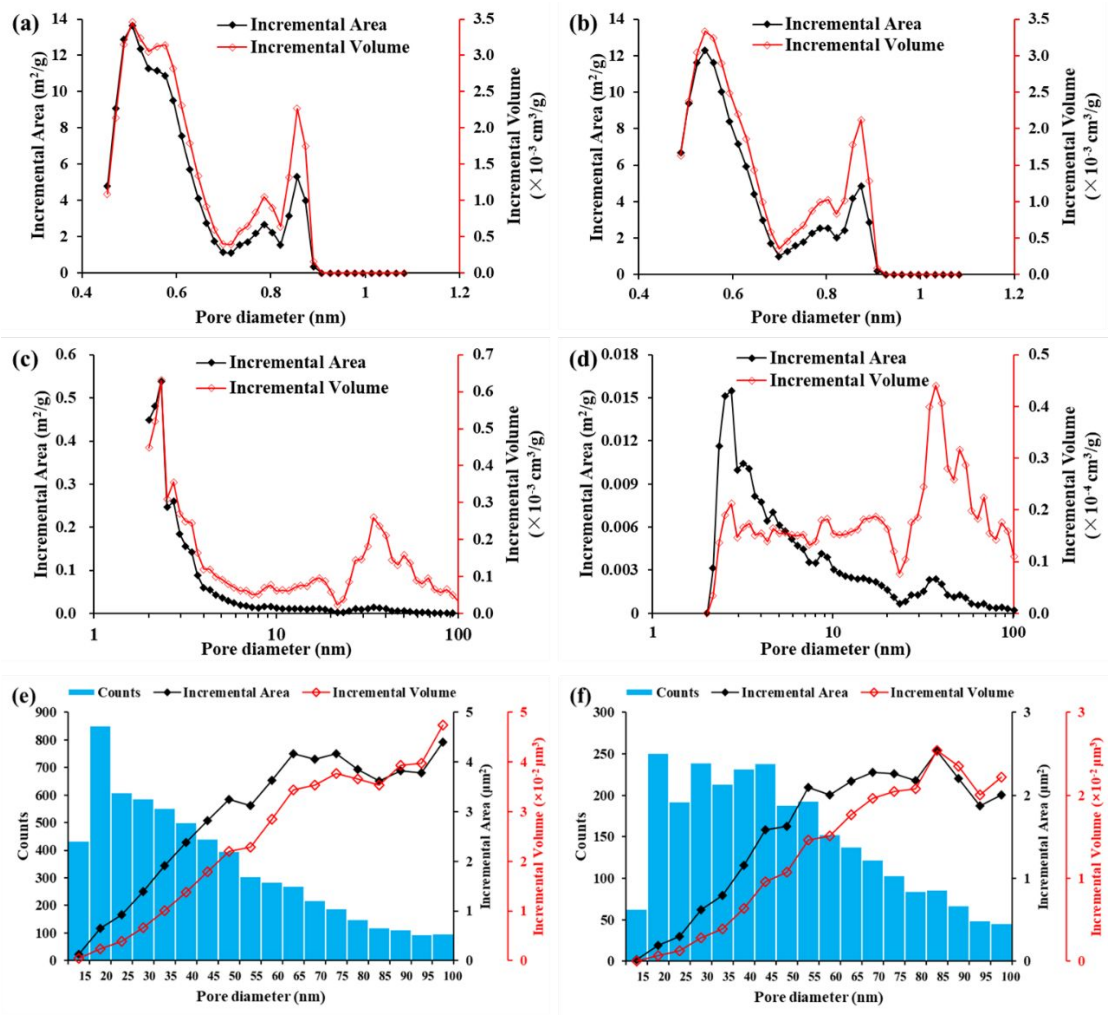

Figure 2. Pore size distribution curves from CO_2 adsorption (a-b), N_2 adsorption (c-d) and FIB-SEM experiment (e-f). The left is sample LHG and the right is sample L-1.

Figure 2 shows the PSD curves of gas adsorption (CO_2 and N_2) and FIB-SEM experiments, which indicate the nanopores from micropores to macropores are developed in two samples. The detecting nanopores from three techniques exhibit various curves due to the distinct principles (including the limited resolution of FIB-SEM and the existence of dead pores). The pore structure parameters from the experiments were summarized in Table 2. The information detected by CO_2 adsorption shows

that the micropores of the two samples are both well-developed, with a large specific surface area up to 121.70-144.48 m^2/g. And the results of N_2 adsorption reveal that the mesopores contribute the most to the pore volume and SSA, followed by the macropores. The data of FIB-SEM shows that the contribution of macropores is the larger.

Table 2. Pore structure information from CO_2 adsorption, N_2 adsorption and FIB-SEM experiments

Sample ID	N_2 adsorption		PVF (%)		SSAF (%)		CO_2 adsorption		FIB-SEM		PVF (%)		SAF (%)	
	PV*	SSA*	meso	macro	meso	macro	PV*	SSA*	PV**	SSA**	meso	macro	meso	macro
LHG	0.00687	2.667	90.20	9.80	99.26	0.74	0.0431	144.48	0.434	52.06	17.76	82.24	25.81	74.19
L-1	0.00098	0.193	79.59	20.41	97.41	2.59	0.0381	121.70	0.235	27.91	15.09	84.91	22.58	77.42

Note: PVF-Pore volume fraction, %; SSAF-Specific surface area fraction, %; SAF-Specific area fraction, %; PV*-pore volume, cm^3/g; SSA*-specific surface area, m^2/g; PV**-pore volume, μm^3; SSA**-specific surface area, μm^2; meso-mesopore; macro-macropore.

Figure 3 shows the characteristics of pores in 2D FIB-SEM slices of two samples. In particular, Figure 3b displays a typical example of multi-level pore transport channel. It can be clearly observed that the body of the channel is composed of multi-level pores, and the connected parts are constituted by narrow throats. The nanopores scattered around provide space for CH_4 adsorption. As illustrated in Figure 4, the nanopores of different sizes will be extracted from the data obtained by FIB-SEM to reconstruct 3D volume and visualize the spatial distribution features. From Figure 2e-f and Figure 4, it can be concluded that the number of nanopores at different sizes in sample LHG is markedly more than that in sample L-1. The mesopores and macropores (see Figure 4a-d) relatively dispersed in space constitute the main storage space of methane, which is consistent with the 2D observation. After analyzing the connectivity of pores (see Figure 4e-f), it is indicated that the connectivity of pores in the selected domain of sample LHG is better, whereas the connected pores appear in the magnified domain of sample L-1. Besides, the connected parts are mainly composed of pores larger than 100 nm. Previous studies have confirmed that nanopores are mainly used as storage space for methane rather than migration channel [19, 22], thus connectivity is not the main characteristic. The

pores above 100 nm will serve as a bridge to transport the desorbed methane to fracture network during the industrial production process.

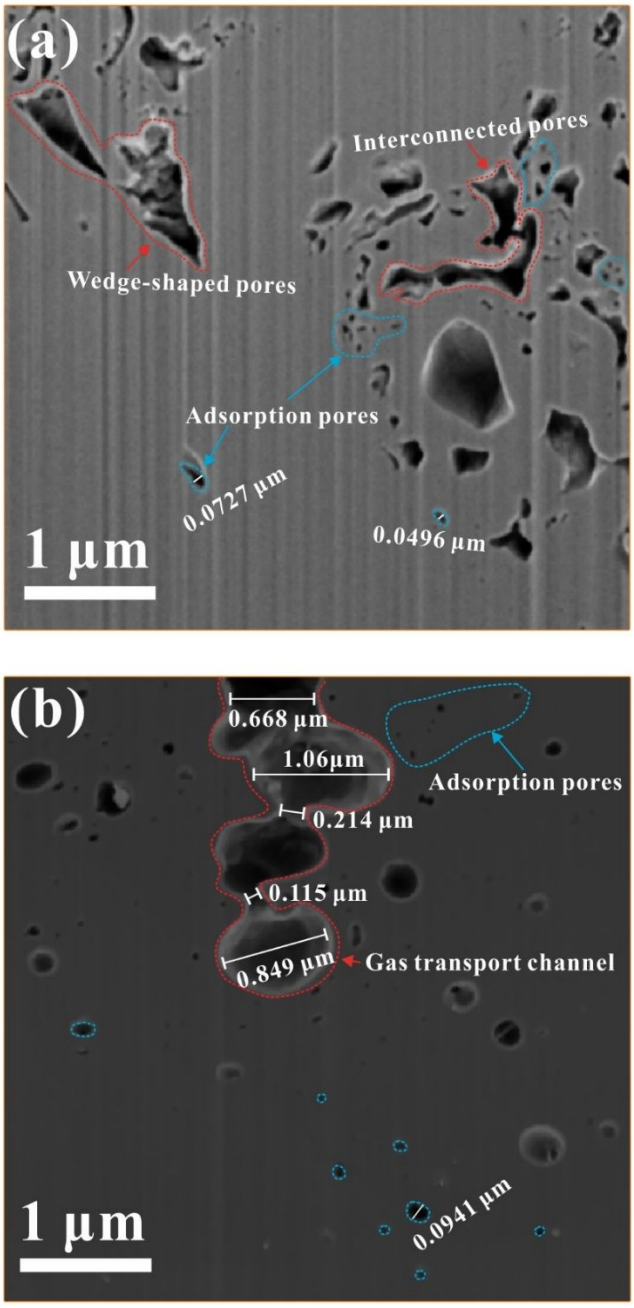

Figure 3. The pore characteristics from samples LHG (a) and L-1 (b) based on 2D slices in FIB-SEM tomography. (a) shows various pore morphologies and adsorption pores. (b) exhibits a typical multi-level transport channel.

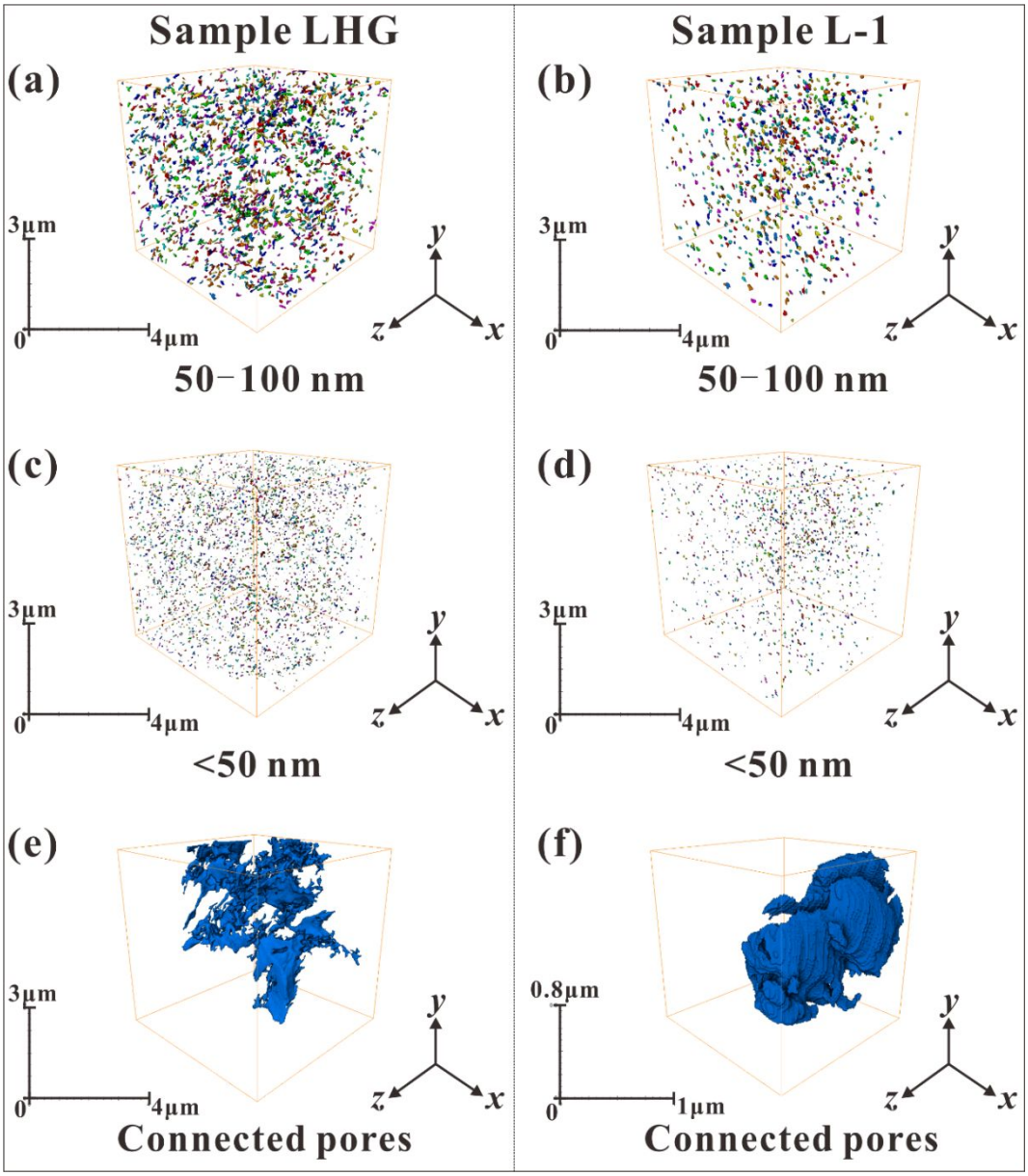

Figure 4. The 3D characteristic spatial distribution of nano-scale pores and connected pores. The left and right columns are sample LHG and sample L-1, respectively. (a) and (b) are the pores with pore diameter ranging from 50-100 nm; (c) and (d) are the pores with pore diameter less than 50nm; (e) and (f) are the connected pores of selected regions.

3.2. Multifractal Analysis from Gas Adsorption Experiments and FIB-SEM Tomography

The nanopores obtained from gas adsorption (CO_2 and N_2) isotherms and FIB-SEM data are rather heterogeneous in the selected samples. The multifractal analysis, a powerful tool for heterogeneity analysis, can be used to reveal these experimental data contained additional information [33, 36, 38, 43, 51]. The different results of CO_2/N_2 adsorption and FIB-SEM are described separately here.

3.2.1 Gas Adsorption Experiments

Based on the calculated results from CO_2/N_2 adsorption experiments, the double logarithmic curves of the partition function $u_i(q,\varepsilon)$ and the measurement scale ε ranging from -10 to 10 of the successive intervals of q=1 are drawn in Figure 5, and it can be found that there is a significant linear relationship (R^2 value > 0.90). Previous studies have confirmed that if the relationship between $u_i(q,\varepsilon)$ and ε obeys a power-law scaling, multifractal behavior can be captured in the PSD of the two samples ranging from micropores to mesopores and macropores [43, 45, 52]. The law of lnε-ln$u(q,\varepsilon)$ is completely opposite when q<0 and q>0, showing a decreasing and increasing trend, respectively. And the fitting lines close to each other indicate that most of the data are clustered in the small domain of the research scale [33, 43]. The generalized multifractal dimension spectrum constituted by D_q and q display a monotonously decreasing curve and $D_0 > D_1 > D_2$, which also supports the existence of multifractal behavior in the nanopores. Parts of parameters are summarized in Table 3. The closer the value of D_1 is to D_0, the more even the pores are distributed in a specific pore size range. Conversely, the smaller value of D_1 represents the denser pores and the more uneven pore distribution [45]. Table 3 shows that the D_1 of samples LHG and L-1 are 0.9067 and 0.9243 in the micropores, which means that the micropore distribution of sample LHG is more uneven. In the meso-macropores detected by the N_2 adsorption experiment, the D_1 value of sample LHG is 0.6191, which is lower than the sample L-1 with 0.7583, indicating the former has a more complex distribution of meso-macropore structure. The H value (Hurst exponent) can be adopted to evaluate the connectivity of pores in the PSD at different sizes, which may further affect the permeability [33]. A smaller H value corresponds to poor pore connectivity. As shown in Table 3, the H values of the micropores are 0.8953 (for sample LHG) and 0.9192 (for sample L-1), representing that the

connectivity of the micropores in sample L-1 is better. The H values of the meso-macropore are 0.6932 (for sample LHG) and 0.7689 (for sample L-1), indicating that the pore connectivity with the range of 2-100 nm in sample L-1 is better. This phenomenon may be related to the plate/slit-like pore shape in sample L-1. The connected channels may be more likely to be produced in plate-liked aggregates, and the narrow necks of ink-bottle pores are not conducive to connectivity.

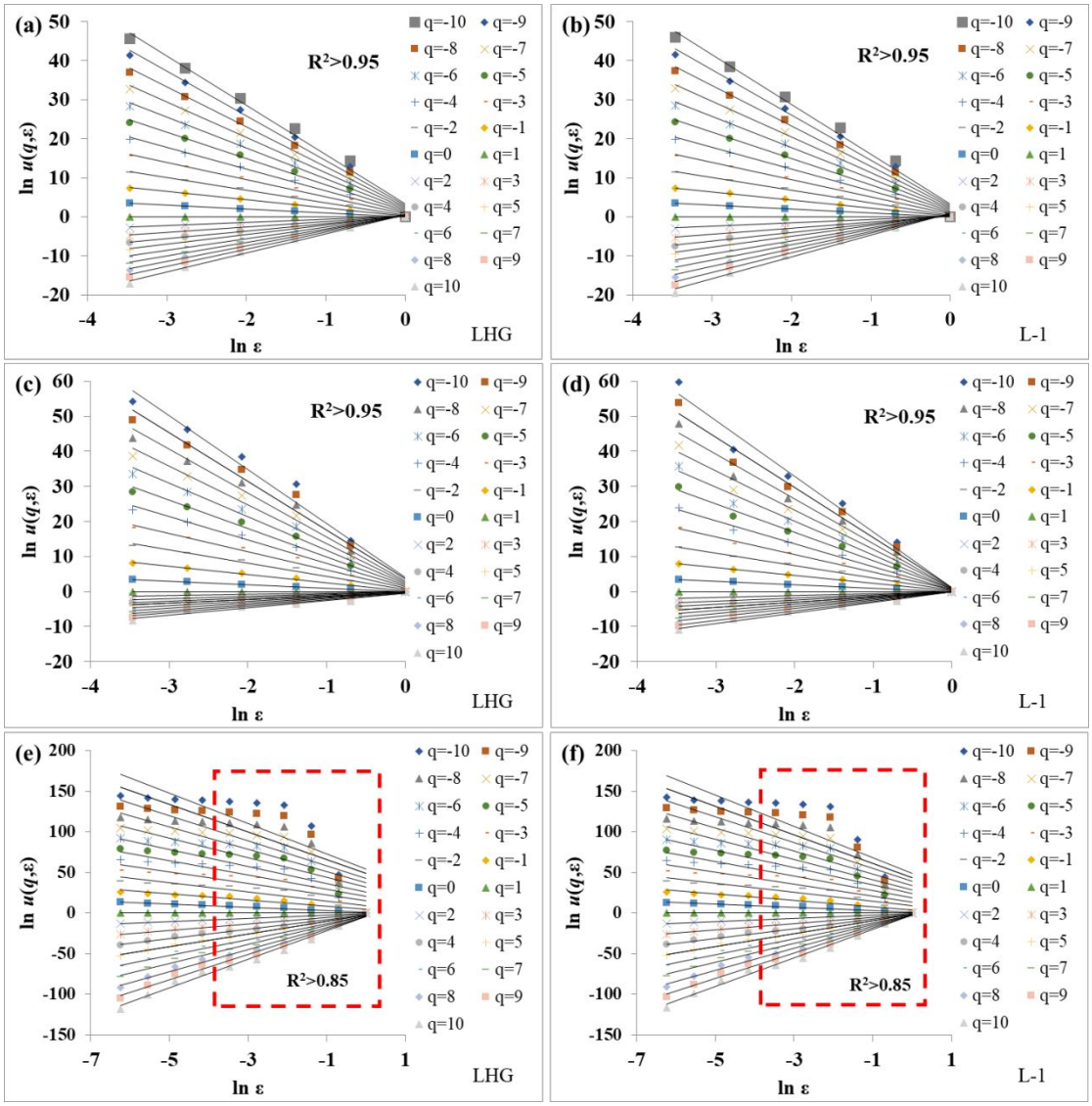

Figure 5. Plots of the partition function at different order q from CO_2 adsorption (a-b), N_2 adsorption (c-d) and FIB-SEM experiments (e-f).

Table 3. Multifractal analysis parameters from CO_2 adsorption, N_2 adsorption and FIB-SEM experiments

Parameters	CO_2 adsorption		N_2 adsorption		FIB-SEM	
	LHG	L-1	LHG	L-1	LHG	L-1
D_0	1.000	1.000	1.000	1.000	2.679	2.657
D_1	0.907	0.924	0.596	0.758	2.485	2.465
D_2	0.791	0.838	0.357	0.538	2.384	2.366
H	0.895	0.919	0.678	0.769	1.692	1.683
D_{10-}-D_{10+}	0.605	0.538	1.207	1.115	1.527	1.574
D_{10-}-D_0	0.152	0.162	0.417	0.445	0.979	1.044
D_0-D_{10+}	0.453	0.376	0.791	0.670	0.548	0.530
α_0	1.070	1.062	1.273	1.175	2.948	2.936
R_d	0.447	0.344	0.870	0.491	0.058	-0.015

The spectrum width of the generalized multifractal dimension spectrum ($D_{10-} \sim D_{10+}$) can reflect the degree of heterogeneity of PSD in a local area, which the higher value corresponds the stronger heterogeneity of PSD within a certain pore size range. As displayed in Table 3, the micropores and meso-macropores in the sample LHG have the larger spectrum width, indicating that the pores in the sample LHG are more heterogeneous in the range of <100 nm. This result confirms the rationality of the D_1 analysis. Besides, the spectrum widths on the left ($D_{10-} \sim D_0$, q<0) and right ($D_0 \sim D_{10+}$, q>0) can show the characteristics of the low-value area and high-value area of the pore volume, respectively [45]. Figure 2a-b demonstrate that the maximum pore volume in the micropores is between 0.45-0.70 nm, and the pore volume in this range is greater than 0.70-1.08 nm. Thus, it can be judged that $D_{10-} \sim D_0$ and $D_0 \sim D_{10+}$ can represent pore heterogeneity in the range of 0.7-1.08 nm and 0.45-0.70 nm, respectively. In the selected samples, the pores ranging from 0.45 to 0.70 nm are more heterogeneous than that of in the range of 0.70-1.08 nm. The same procedure may be easily utilized to find that the left and right spectrum widths in meso-macropores indicate pore heterogeneity in the range of 50-100 nm and 2-50 nm, respectively. Obviously, Figure 6 displays that the right spectrum width is larger than that on the left in micropore and meso-macropore of the

two samples, which means the distribution in the range of 2-50 nm is more complex.

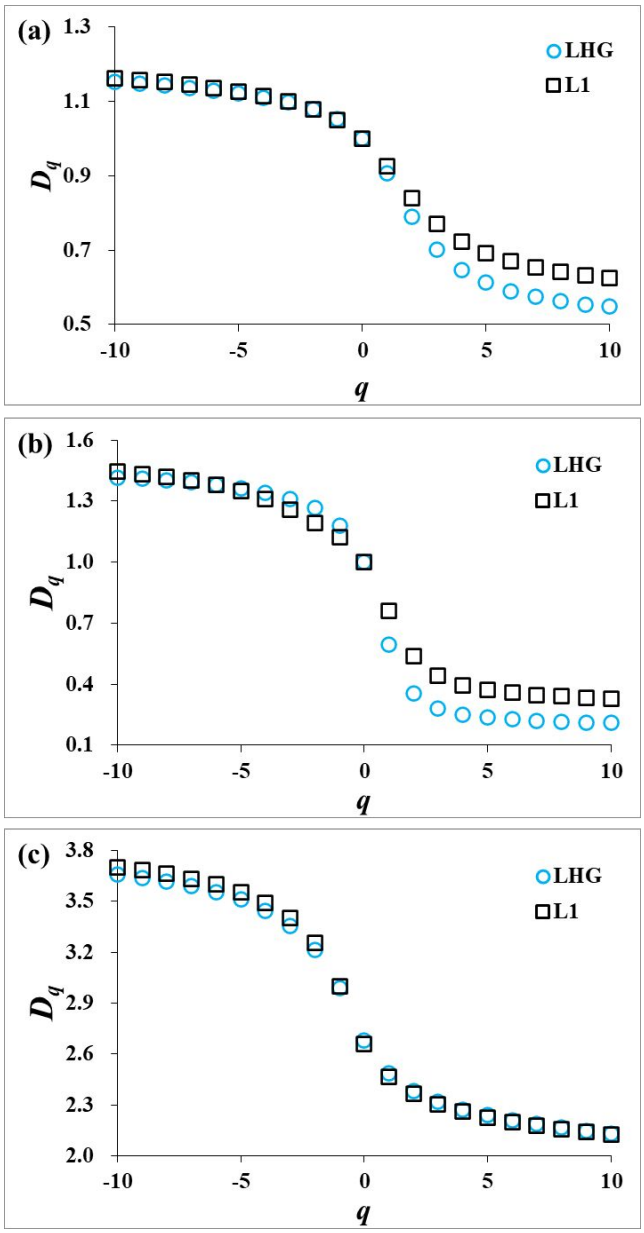

Figure 6. Relation between the generalized dimension (D_q) and the moment order (q) of the samples from CO_2 adsorption (a), N_2 adsorption (b) and FIB-SEM experiments (c).

Another important element is the multifractal singular spectrum [α, $f(\alpha)$] presenting an upwardly convex parabolic shape, which proves the multifractal behavior of PSDs in these samples [33, 53]. This curve is tangent to the internal bisector $f(\alpha)=\alpha$ (see Figure 7) [36], which confirms the accuracy of our calculation. The parameter α_0 is used, which its higher value is regarded as more obvious local agglomeration of pores, to reflect the degree of concentration of PSD. The results in Table 3 indicate

that the PSD concentration of micropores and meso-macropores of sample LHG is higher than that of sample L-1. Here R_d is used to observe the deviation degree of the multifractal singular spectrum from the center, that is, $R_d=[(\alpha_0-\alpha_{10+})-(\alpha_{10-}-\alpha_0)]$ [54]. The results show $R_d>0$ in micropores and meso-macropores, which means that the high probability density region of pores significantly affects the pore volume distribution. Besides, the relation between $\tau(q)$ and q displayed in Figure 8 demonstrate increasing convex curves in the three experiments, which is consistent with the characteristics of multifractal analysis. Compared with $q>0$, the increasing trend is more significant when $q<0$.

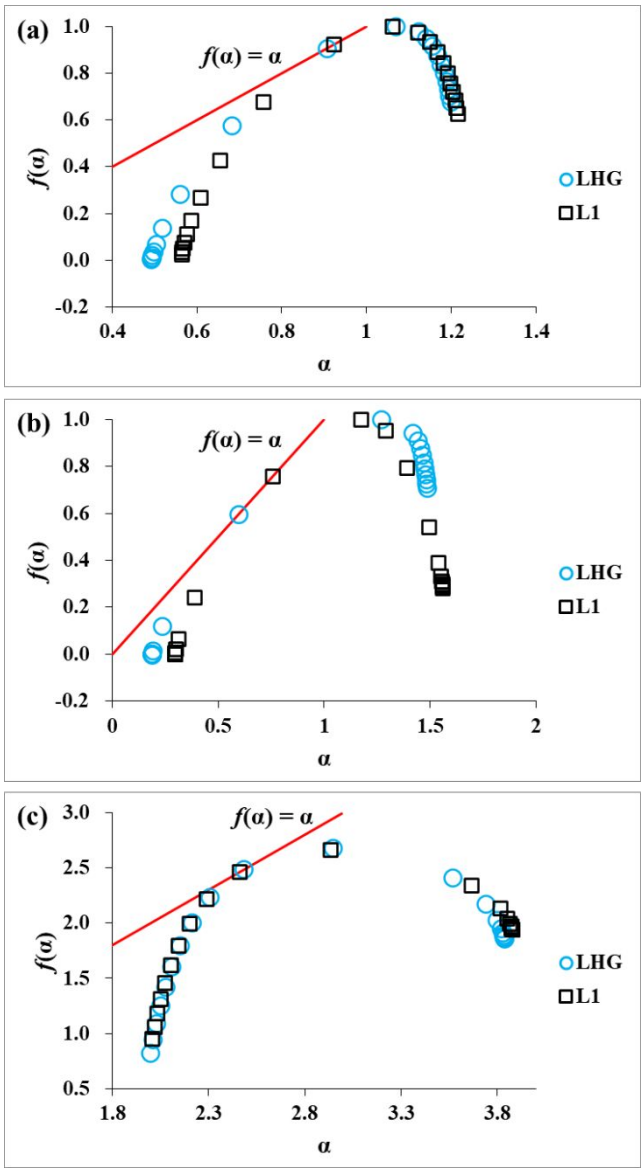

Figure 7. The multifractal singularity spectra [$f(\alpha)$- α] of the selected samples from CO_2 adsorption (a), N_2 adsorption (b) and FIB-SEM experiments (c). And the red line is $f(\alpha) = \alpha$. The curve of [$f(\alpha)$- α] being

tangent to the line of $f(\alpha)=\alpha$ proves the accuracy of the calculation.

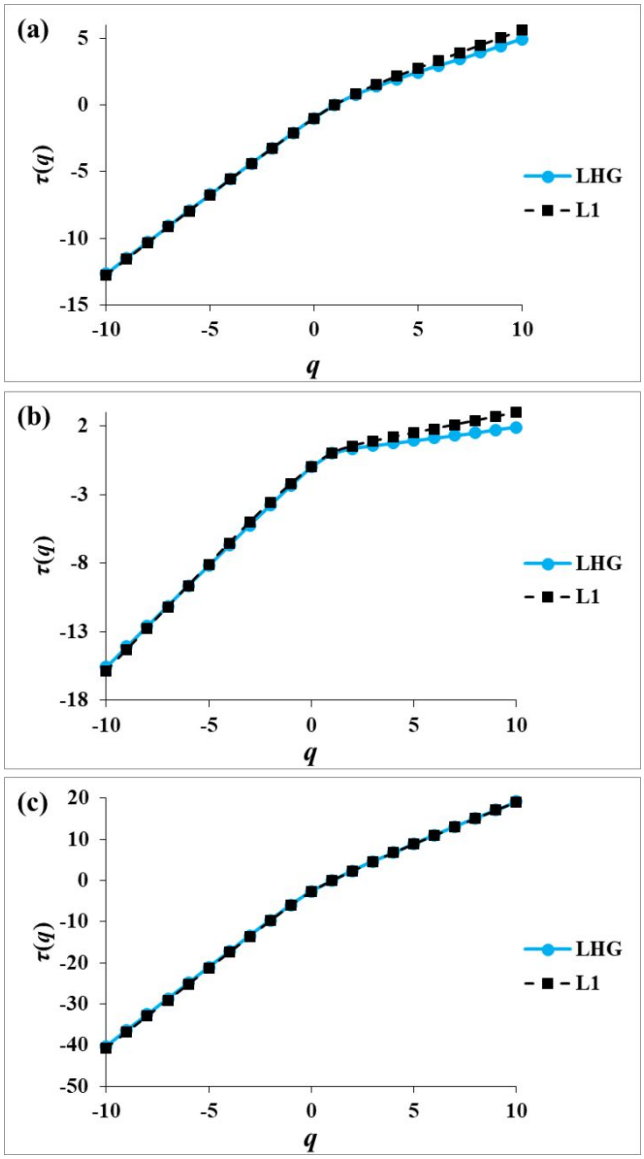

Figure 8. Relation between $\tau(q)$ and q from CO_2 adsorption (a), N_2 adsorption (b) and FIB-SEM experiments (c).

3.2.2 FIB-SEM Tomography

Prior to perform FIB-SEM multifractal analysis, a key step is to determine the range of scale used for calculation [51, 55]. The maximum scales of the selected samples are 512 × 512 × 512 voxels, but the minimum scales should also be determined. This depends on the nearly linear part of the bi-log plots of partition function $u(q,\varepsilon)$ and ε illustrated in Figure 5. Therefore, unlike linear correlation coefficients $R^2>0.95$ in CO_2 adsorption and N_2 adsorption isotherms, the R^2 values of the linear part in FIB-SEM are accepted to be greater than 0.85 (see the red rectangular frames in Figure 5e-f). The

minimum scale is set to 2^4 pixels. Only nanopores smaller than 100 nm are selected and analyzed in FIB-SEM experiment, resulting in not all boxes containing pores. Therefore, D_0 is not equal to 3, but a value between 2-3. Both the monotonic decrease in Figure 6c and the monotonic increase in Figure 8c capture the multifractal behavior of the PSD in FIB-SEM. A higher H value indicates better connectivity between the pores in the sample LHG. It differs from the results of the N_2 adsorption analysis, which may be due to the limited resolution that cannot detect pores below 10 nm, leading to underestimate pore connectivity of the sample L-1. It also demonstrates that the pores of 2-10 nm may act as the medium connecting the pores. Combining Table 2 and Fig 2e-f, it can be concluded that the left side (D_{10-}~D_0, q<0) and the right side (D_0~D_{10+}, q>0) reflect the features of pores in the range of 10-50 nm and 50-100 nm, respectively. The spectrum width on the left is larger than that on the right shown in Table 3, which means that the pore heterogeneity of 10-50 nm is stronger. The α_0 value of sample LHG is slightly higher than that of sample L-1, indicating that the local agglomeration of pores in the former is more obvious. Table 3 shows that the R_d of sample LHG is greater than 0, while the R_d of sample L-1 is less than 0, indicating that their PSDs are dominated by the high probability density area and the low probability density area, respectively. Besides, it is worth noting that the parameter difference of N_2 adsorption is more significant than that of FIB-SEM. This may include two reasons: 1) the limited resolution of FIB-SEM cannot detect pores of 2-10 nm; 2) N_2 adsorption only focuses on open pores, but FIB-SEM will also show closed pores.

3.3. Impacts of The Nanopores on Methane Adsorption

The samples LHG and L-1 were collected from Junggar Basin and Qinshui Basin, which are two active and typical CBM areas in China [56, 57]. Lots of previous studies have indicated that the coal

samples in these two basins are markedly various (as shown in Table 4) [27, 56-58]. Therefore, these selected samples are representative to compare the differences of pore structures between a high volatile bituminous coal and an anthracite. The V_L values are 43.37 m^3/t (sample LHG) and 38.37 m^3/t (sample L-1) as shown in Table 1, meaning the great CH_4 adsorption capacity. Previous studies showed that the high-rank coals tend to have higher CH_4 enrichment capacity compared with low-rank coals [6-8]. Nevertheless, the methane adsorption capacity of sample LHG (high volatile bituminous coal) is stronger than that of sample L-1 (anthracite) in our study. It should be started with the pore characteristics to explore the direct cause of this phenomenon. The first thing to note is when the volume and SSA of pores with size of 2-100 nm in sample L-1 are several orders of magnitude lower than those of sample LHG (see Table 2), the V_L value of sample L-1 can still be as high as 34.81 m^3/t. As illustrated in Figure 9, the micropore occupies an absolute dominant position in both pore volume and SSA. The larger SSA can provide more adsorption sites for methane [13]. Thus, this phenomenon can be attributed to the quite developed micropore system, which is similar to previous research [13, 16, 46]. However, the expansion of coal may occur during the process of CO_2 adsorption [56], so it cannot be used as the only criterion. Therefore, what we should focus on next is the type of pore morphology, affecting the gas enrichment and diffusion [59]. The N_2 adsorption/desorption curves in Figure 1c show that narrow slit-like pores easily exist in the sample LHG with higher SSA. This pore structure is conducive to gas storage, but may hinder the desorption and diffusion of CBM. The pore morphology in sample L-1 presents non-grid aggregates of plate-like particles (Figure 1d), which will facilitate the desorption and diffusion of gas but is not beneficial to the gas adsorption and storage. But Cai et al. showed that the pore morphology type that is favorable for gas adsorption does not necessarily correspond to higher CH_4 adsorption

capacity [19]. In other words, the methane adsorption may still be restricted by other factors. Lozano-Castello et al. [15] and Wei et al. [16] revealed that gas adsorption capacity was positively correlated with micropore volume. Further studies investigated that the methane adsorption was not only limited by the micropore volume, but also greatly affected by the micropore size distribution [17, 18]. Multifractal theory establishes a finely quantified bridge between PSD and heterogeneity. The multifractal behavior in PSD of nanopore at multiple scales has been confirmed in Section 3.2, which can be utilized for fine contrast of heterogeneity. The 2D characteristics of CO_2 and N_2 adsorption indicate that the PSD in the range of 0.45-0.70 nm and 2-50 nm of sample LHG is more complicated comparing with sample L-1. Due to the 3D spatial distribution properties obtained by FIB-SEM, the pore heterogeneity in the 10-50 nm range of sample L-1 is stronger than that of sample LHG. This may be because the closed pores are taken into consideration by FIB-SEM. The CH_4 adsorption isotherm experiment conducted in this work may not be able to fully study the effect of closed pores, but mainly focuses on open pores. Hence according to the multifractal results, it can be inferred that the stronger pore heterogeneity in the range of 0.45-0.70 nm and 2-50 nm is beneficial for methane adsorption.

Although the detailed work on the effect of nanopores on CH_4 adsorption performance between a high volatile bituminous coal and an anthracite has been discussed, the number of samples is not sufficient to consider and explore all features of coals. Therefore, we will collect more samples to conduct systematic experiments, thereby establishing a multi-factor quantitative model in the next work.

Table 4. Differences of the coal parameters in Junggar Basin and Qinshui Basin

Previous research	R_o (%)		Porosity (%)	
	Junggar Basin	Qinshui Basin	Junggar Basin	Qinshui Basin
Wang et al. [60],	0.35-0.84	1.83-4.26	6.2-14.0	2.2-6.9
Li et al. [56],	0.42-0.59	2.95-3.10	-	-
Cai et al. [27],	0.49-0.72	1.78-2.95	6.0-20.8	4.34-12.12
Fu et al. [58],	0.52-0.88	-	3.13-9.78	-

Note: "-" is none.

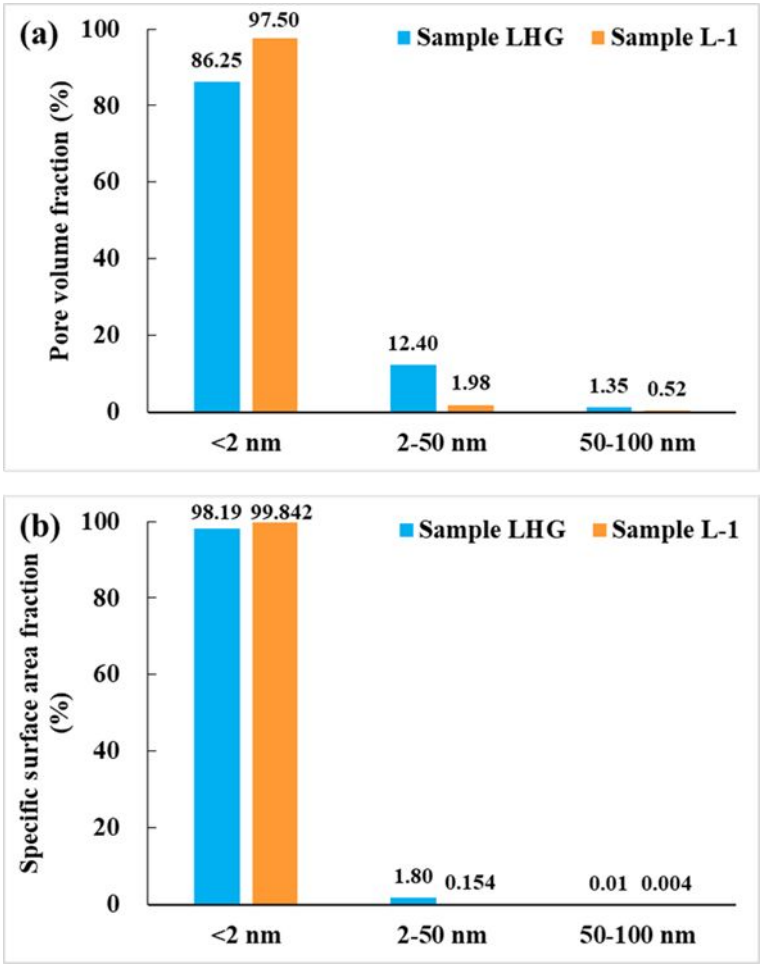

Figure 9. The proportion of pore volume and specific surface area in the nanopore structure. (a)-pore volume fraction; (b)-specific surface area fraction.

4. CONCLUSIONS

In this work, a combined conventional CO_2 adsorption at 273 K, N_2 adsorption at 77 K and unconventional FIB-SEM tomography analysis have been conducted on high volatile bituminous coal and anthracite. The effect of nanopores on CH_4 adsorption capacity was discussed by using

multi-dimensional multifractal analysis. The following conclusions can be made.

1) The combination of gas adsorption (CO_2 and N_2) and FIB-SEM can extend the fine description of the nanopore structure from two-dimensional to three-dimensional. And FIB-SEM shows that the nanopores are isolated in the space, indicating that they are mainly used as a storage section.

2) The multifractal behavior has been captured in the detected various pore size distributions from gas adsorption (CO_2 and N_2) and FIB-SEM. The nanopores of the sample LHG have stronger heterogeneity in multiple dimensions. More precisely, the areas where pore aggregation is prominent include 0.45-0.70 nm (from CO_2 adsorption), 2-50 nm (from N_2 adsorption) and 10-50 nm (from FIB-SEM).

3) The effect of nanopore structure on methane adsorption capacity revolves around micropore structure, pore morphology and heterogeneity. The well-developed micropore structure is favorable to methane enrichment. The ink-bottle pores with higher SSA are conducive to gas storage but may hinder the desorption and diffusion of CBM. The pore morphology presenting plate-like particle aggregates with slit-like pores will facilitate the desorption and diffusion of gas and is not beneficial to the gas adsorption. The stronger pore heterogeneity in the range of 0.45-0.70 nm and 2-50 nm is beneficial for methane adsorption.

ACKNOWLEDGEMENTS

This research was funded by the National Natural Science Foundation of China (grant numbers 41830427, 41922016, and 41772160).

REFERENCES

(1) Gray, I., Reservoir engineering in coal seams: Part 1-The physical process of gas storage and movement in coal seams. *SPE Reservoir Eng* **1987,** 2(01), 28-34.

(2) Zhou, Y. B.; Zhang, R. L.; Wang, J.; Huang, J. L.; Li, X. R.; Wu, J. G., Desorption hysteresis of CO2 and CH4 in different coals with cyclic desorption experiments. *J. CO2 Util.* **2020,** 40, 101200.

(3) Naveen, P.; Asif, M.; Ojha, K., Integrated fractal description of nanopore structure and its effect on CH4 adsorption on Jharia coals, India. *Fuel* **2018,** 232, 190-204.
(4) Busch, A.; Gensterblum, Y., CBM and CO2-ECBM related sorption processes in coal: A review. *Int. J. Coal Geol.* **2011,** 87(2), 49-71.
(5) Liu, J.; Zhang, R.; Song, D. H.; Wang, Z. Q., Experimental investigation on occurrence of gassy coal extrusion in coalmine. *Safety. Sci.* **2019,** 113, 362-371.
(6) Merkel, A.; Gensterblum, Y.; Krooss, B. M.; Amann, A., Competitive sorption of CH4, CO2 and H2O on natural coals of different rank. *Int. J. Coal Geol.* **2015,** 150, 181-192.
(7) Gensterblum, Y.; Merkel, A.; Busch, A.; Krooss, B. M., High-pressure CH4 and CO2 sorption isotherms as a function of coal maturity and the influence of moisture. *Int. J. Coal Geol.* **2013,** 118, 45-57.
(8) Hildenbrand, A.; Krooss, B. M.; Busch, A.; Gaschnitz, R., Evolution of methane sorption capacity of coal seams as a function of burial history - A case study from the Campine Basin, NE Belgium. *Int. J. Coal Geol.* **2006,** 66(3), 179-203.
(9) Zhang, J. F.; Clennell, M. B.; Dewhurst, D. N.; Liu, K. Y., Combined Monte Carlo and molecular dynamics simulation of methane adsorption on dry and moist coal. *Fuel* **2014,** 122, 186-197.
(10) Crosdale, P. J.; Beamish, B. B.; Valix, M., Coalbed methane sorption related to coal composition. *Int. J. Coal Geol.* **1998,** 35(1-4), 147-158.
(11) Bustin, R. M.; Clarkson, C. R., Geological controls on coalbed methane reservoir capacity and gas content. *Int. J. Coal Geol.* **1998,** 38(1-2), 3-26.
(12) Tao, S.; Chen, S. D.; Tang, D. Z.; Zhao, X.; Xu, H.; Li, S., Material composition, pore structure and adsorption capacity of low-rank coals around the first coalification jump: A case of eastern Junggar Basin, China. *Fuel* **2018,** 211, 804-815.
(13) Zhao, J. L.; Xu, H.; Tang, D. Z.; Mathews, J. P.; Li, S.; Tao, S., A comparative evaluation of coal specific surface area by CO2 and N-2 adsorption and its influence on CH4 adsorption capacity at different pore sizes. *Fuel* **2016,** 183, 420-431.
(14) Liu, X. F.; He, X. Q., Effect of pore characteristics on coalbed methane adsorption in middle-high rank coals. *Adsorption* **2017,** 23(1), 3-12.
(15) Lozano-Castello, D.; Cazorla-Amoros, D.; Linares-Solano, A., Powdered activated carbons and activated carbon fibers for methane storage: A comparative study. *Energy Fuels* **2002,** 16(5), 1321-1328.
(16) Wei, Q.; Li, X. Q.; Zhang, J. Z.; Hu, B. L.; Zhu, W. W.; Lian, W. L.; Sun, K. X., Full-size pore structure characterization of deep-buried coals and its impact on methane adsorption capacity: A case study of the Shihezi Formation coals from the Panji Deep Area in Huainan Coalfield, Southern North China. *J. Petrol. Sci. Eng.* **2019,** 173, 975-989.
(17) Lozano-Castello, D.; Cazorla-Amoros, D.; Linares-Solano, A.; Quinn, D. F., Influence of pore size distribution on methane storage at relatively low pressure: preparation of activated carbon with optimum pore size. *Carbon* **2002,** 40(7), 989-1002.
(18) Lozano-Castello, D.; Cazorla-Amoros, D.; Linares-Solano, A.; Quinn, D. F., Micropore size distributions of activated carbons and carbon molecular sieves assessed by high-pressure methane and carbon dioxide adsorption isotherms. *J. Phys. Chem. B* **2002,** 106(36), 9372-9379.
(19) Cai, Y. D.; Liu, D. M.; Pan, Z. J.; Yao, Y. B.; Li, J. Q.; Qiu, Y. K., Pore structure and its impact on CH4 adsorption capacity and flow capability of bituminous and subbituminous coals from Northeast China. *Fuel* **2013,** 103, 258-268.
(20) Yao, Y. B.; Liu, D. M.; Tang, D. Z.; Tang, S. H.; Huang, W. H., Fractal characterization of

adsorption-pores of coals from North China: An investigation on CH4 adsorption capacity of coals. *Int. J. Coal Geol.* **2008,** 73(1), 27-42.
(21) IUPAC, Reporting physisorption data for gas/solid systems with special reference to the determination of surface area and porosity. *Pure Appl. Chem.* **1982,** 54, 2201-2218.
(22) Zhou, S. D.; Liu, D. M.; Cai, Y. D.; Karpyn, Z.; Yao, Y. B., Comparative analysis of nanopore structure and its effect on methane adsorption capacity of Southern Junggar coalfield coals by gas adsorption and FIB-SEM tomography. *Micropor. Mesopor. Mat.* **2018,** 272, 117-128.
(23) Shan, C. A.; Zhang, T. S.; Liang, X.; Shu, D. C.; Zhang, Z.; Wei, X. F.; Zhang, K.; Feng, X. L.; Zhu, H. H.; Wang, S. T.; Chen, Y., Effects of nano-pore system characteristics on CH4 adsorption capacity in anthracite. *Frontiers of Earth Science* **2019,** 13(1), 75-91.
(24) Hu, B.; Cheng, Y. P.; He, X. X.; Wang, Z. Y.; Jiang, Z. N.; Wang, C. H.; Li, W.; Wang, L., New insights into the CH4 adsorption capacity of coal based on microscopic pore properties. *Fuel* **2020,** 262, 116675.
(25) Byamba-Ochir, N.; Shim, W. G.; Balathanigaimani, M. S.; Moon, H., High density Mongolian anthracite based porous carbon monoliths for methane storage by adsorption. *Appl. Energy* **2017,** 190, 257-265.
(26) Gan, H.; Nandi, S. P.; Walker Jr, P. L., Nature of the porosity in American coals. *Fuel* **1972,** 51(4), 272-277.
(27) Cai, Y. D.; Li, Q.; Liu, D. M.; Zhou, Y. F.; Lv, D. W., Insights into matrix compressibility of coals by mercury intrusion porosimetry and N-2 adsorption. *Int. J. Coal Geol.* **2018,** 200, 199-212.
(28) Clarkson, C. R.; Solano, N.; Bustin, R. M.; Bustin, A. M. M.; Chalmers, G. R. L.; He, L.; Melnichenko, Y. B.; Radlinski, A. P.; Blach, T. P., Pore structure characterization of North American shale gas reservoirs using USANS/SANS, gas adsorption, and mercury intrusion. *Fuel* **2013,** 103, 606-616.
(29) Thommes, M.; Kaneko, K.; Neimark, A. V.; Olivier, J. P.; Rodriguez-Reinoso, F.; Rouquerol, J.; Sing, K. S. W., Physisorption of gases, with special reference to the evaluation of surface area and pore size distribution (IUPAC Technical Report). *Pure Appl. Chem.* **2015,** 87(9-10), 1051-1069.
(30) Akbarabadi, M.; Saraji, S.; Piri, M.; Georgi, D.; Delshad, M., Nano-scale experimental investigation of in-situ wettability and spontaneous imbibition in ultra-tight reservoir rocks. *Adv. Water Resour.* **2017,** 107, 160-179.
(31) International Committee for Coal and Organic Petrology (ICCP)., The new vitrinite classifcation (ICCP System 1994). *Fuel* **1998,** 77(5), 349–358.
(32) Do, D. D.; Do, H. D., Pore characterization of carbonaceous materials by DFT and GCMC simulations: A review. *Adsorpt. Sci. Technol.* **2003,** 21(5), 389-423.
(33) Liu, K. Q.; Ostadhassan, M.; Zou, J.; Gentzis, T.; Rezaee, R.; Bubach, B.; Carvajal-Ortiz, H., Multifractal analysis of gas adsorption isotherms for pore structure characterization of the Bakken Shale. *Fuel* **2018,** 219, 296-311.
(34) Song, D. Y.; Ji, X. F.; Li, Y. B.; Zhao, H. T.; Song, B. Y.; He, K. K., Heterogeneous development of micropores in medium-high rank coal and its relationship with adsorption capacity. *Int. J. Coal Geol.* **2020,** 226, 103497.
(35) Langmuir, I., The constitution and fundamental properties of solids and liquids. Part I. Solids. *JACS* **1916,** 38(11), 2221-2295.
(36) Karimpouli, S.; Tahmasebi, P., 3D multi-fractal analysis of porous media using 3D digital images: considerations for heterogeneity evaluation. *Geophys. Prospect.* **2019,** 67(4), 1082-1093.

(37) Li, Q.; Liu, D. M.; Cai, Y. D.; Zhao, B.; Qiu, Y. K.; Zhou, Y. F., Scale-span pore structure heterogeneity of high volatile bituminous coal and anthracite by FIB-SEM and X-ray μ-CT. *J. Nat. Gas Sci. Eng.* **2020,** 81, 103443.
(38) Lopes, R.; Betrouni, N., Fractal and multifractal analysis: A review. *Med. Image Anal.* **2009,** 13(4), 634-649.
(39) Halsey, T. C.; Jensen, M. H.; Kadanoff, L. P.; Procaccia, I.; Shraiman, B. I., Fractal measures and their singularities: the characterization of strange sets. *Physical Review A* **1986,** 33(2), 1141-1151.
(40) Zheng, S. J.; Yao, Y. B.; Liu, D. M.; Cai, Y. D.; Liu, Y.; Li, X. W., Nuclear magnetic resonance T-2 cutoffs of coals: A novel method by multifractal analysis theory. *Fuel* **2019,** 241, 715-724.
(41) Russell, D. A.; Hanson, J. D.; Ott, E., Dimension of strange attractors. *Phys. Rev. Lett.* **1980,** 45(14), 1175–1178.
(42) Chhabra, A.; Jensen, R. V., Direct determination of the f(α) singularity spectrum. *Phys. Rev. Lett.* **1989,** 62(12), 1327-1330.
(43) Ferreiro, J. P.; Wilson, M.; Vazquez, E. V., Multifractal description of nitrogen adsorption isotherms. *Vadose Zone J.* **2009,** 8(1), 209-219.
(44) Caniego, F. J.; Martin, M. A.; San Jose, F., Singularity features of pore-size soil distribution: Singularity strength analysis and entropy spectrum. *Fractals* **2001,** 9(3), 305-316.
(45) Li, W.; Liu, H. F.; Song, X. X., Multifractal analysis of Hg pore size distributions of tectonically deformed coals. *Int. J. Coal Geol.* **2015,** 144, 138-152.
(46) Riedi, R. H.; Crouse, M. S.; Ribeiro, V. J.; Baraniuk, R. G., A multifractal wavelet model with application to network traffic. *IEEE Trans. Inf. Theory* **1999,** 45(3), 992-1018.
(47) Okolo, G. N.; Everson, R. C.; Neomagus, H.; Roberts, M. J.; Sakurovs, R., Comparing the porosity and surface areas of coal as measured by gas adsorption, mercury intrusion and SAXS techniques. *Fuel* **2015,** 141, 293-304.
(48) Yan, J. W.; Meng, Z. P.; Zhang, K.; Yao, H. F.; Hao, H. J., Pore distribution characteristics of various rank coals matrix and their influences on gas adsorption. *J. Petrol. Sci. Eng.* **2020,** 189, 107041.
(49) Han, F. S.; Busch, A.; Krooss, B. M.; Liu, Z. Y.; Yang, J. L., CH4 and CO2 sorption isotherms and kinetics for different size fractions of two coals. *Fuel* **2013,** 108, 137-142.
(50) Sing, K. S. W.; Everett, D. H.; Haul, R. A. W.; Moscou, L.; Pierotti, R. A.; Rouquerol, J.; Siemieniewska, T., Reporting physisorption data for gas solid systems with special reference to the determination of surface-area and porosity. *Pure Appl. Chem.* **1985,** 57(4), 603-619.
(51) Torre, I. G.; Losada, J. C.; Heck, R. J.; Tarquis, A. M., Multifractal analysis of 3D images of tillage soil. *Geoderma* **2018,** 311, 167-174.
(52) Muller, J., Characterization of pore space in chalk by multifractal analysis. *J. Hydrol.* **1996,** 187(1-2), 215-222.
(53) Soto-Gomez, D.; Perez-Rodriguez, P.; Juiz, L. V.; Paradelo, M.; Lopez-Periago, J. E., 3D multifractal characterization of computed tomography images of soils under different tillage management: Linking multifractal parameters to physical properties. *Geoderma* **2020,** 363, 114129.
(54) Song, Y.; Jiang, B.; Shao, P.; Wu, J. H., Matrix compression and multifractal characterization for tectonically deformed coals by Hg porosimetry. *Fuel* **2018,** 211, 661-675.
(55) Saa, A.; Gasco, G.; Grau, J. B.; Anton, J. M.; Tarquis, A. M., Comparison of gliding box and box-counting methods in river network analysis. *Nonlinear Proc. Geoph.* **2007,** 14(5), 603-613.
(56) Li, Y.; Zhang, C.; Tang, D. Z.; Gan, Q.; Niu, X. L.; Wang, K.; Shen, R. Y., Coal pore size distributions controlled by the coalification process: An experimental study of coals from the Junggar,

Ordos and Qinshui basins in China. *Fuel* **2017,** 206, 352-363.
(57) Qin, Y.; Moore, T. A.; Shen, J.; Yang, Z. B.; Shen, Y. L.; Wang, G., Resources and geology of coalbed methane in China: a review. *Int. Geol. Rev.* **2018,** 60(5-6), 777-812.
(58) Fu, H. J.; Tang, D. Z.; Xu, H.; Xu, T.; Chen, B. L.; Hu, P.; Yin, Z. Y.; Wu, P.; He, G. J., Geological characteristics and CBM exploration potential evaluation: A case study in the middle of the southern Junggar Basin, NW China. *J. Nat. Gas Sci. Eng.* **2016,** 30, 557-570.
(59) Li, Z. T.; Liu, D. M.; Cai, Y. D.; Wang, Y. P.; Teng, J., Adsorption pore structure and its fractal characteristics of coals by N-2 adsorption/desorption and FESEM image analyses. *Fuel* **2019,** 257, 116031.
(60) Wang, Y. J.; Liu, D. M.; Cai, Y. D.; Li, X. W., Variation of petrophysical properties and adsorption capacity in different rank coals: An experimental study of coals from the Junggar, Ordos and Qinshui Basins in China. *Energies* **2019,** 12(6), 986.

562 **TOC graphic**

563